Nanoscale

ROYAL SOCIETY OF CHEMISTRY

COMMUNICATION

View Article Online
View Journal | View Issue

Cite this: *Nanoscale*, 2023, **15**, 8611

Received 12th December 2022,
Accepted 14th April 2023

DOI: 10.1039/d2nr06965b

rsc.li/nanoscale

The shape anisotropy of magnetic nanoparticles: an approach to cell-type selective and enhanced internalization†

Tanja Potrč,[a] Slavko Kralj, *[a,b,c] Sebastjan Nemec,[a,b] Petra Kocbek[a] and Mateja Erdani Kreft*[d]

The effects of the shape anisotropy of nanoparticles on cellular uptake is still poorly understood due to challenges in the synthesis of anisotropic magnetic nanoparticles of the same composition. Here, we design and synthesize spherical magnetic nanoparticles and their anisotropic assemblies, namely magnetic nanochains (length ~800 nm). Then, nanoparticle shape anisotropy is investigated on urothelial cells *in vitro*. Although both shapes of nanomaterials reveal biocompatibility, we havefound significant differences in the extent of their intracellular accumulation. Contrary to spherical particles, anisotropic nanochains preferentially accumulate in cancer cells as confirmed by inductively coupled plasma (ICP) analysis, indicating that control of the nanoparticle shape geometry governs cell-type-selective intracellular uptake and accumulation.

Introduction

Magnetic iron oxide nanoparticles have been the subject of intense research in the field of cancer therapy in the past few decades.[1] Magnetic nanoparticles for biomedical applications are usually in the form of small spherical nanocrystals with a size of less than 20 nm in order to preserve their superparamagnetic behavior.[2] Most of the studies in the past two decades have thus focused on magnetic nanoparticles with spherical shape, since they are generally easy to prepare by reproducible experimental procedures.[3] Recently, research interest in magnetic nanoparticles with anisotropic shapes has been growing.[4] Shape anisotropy and magnetocrystalline anisotropy strongly affect the behavior of the nanoparticles in a low frequency alternating magnetic field.[1] These features of magnetic nanoparticles enable their remotely controlled rotational or vibrational movements and hence represent a novel means for advanced drug delivery[5] and cancer treatment based on magneto-mechanical effect.[6]

Nanoparticle geometry has an important effect on cellular uptake and biodistribution.[1] In general, the specific surface area of nanoparticles is increased when the aspect-ratio of the nanoparticles is enlarged at a certain particle volume. Theoretically, non-spherical particles have a larger surface available for adhesive interactions than their spherical counterparts.[7] Therefore, nanoparticles with different morphologies such as cubes, rods,[8] disks,[9] fibers,[10,11] flowers, hollow spheres, worms, stars or tetrapods,[1] and superparamagnetic nanostructures with highly anisotropic shapes, *i.e.* nanochains,[12] can exert multiple interactions with cell membranes, which might result in a larger extent of nanoparticle internalization.[1] It is also known that nanomaterials with high aspect ratio geometries show longer blood circulation times compared to spherical particles.[1,10] The functionalization of non-spherical particles can also act in synergy with non-spherical shape to extend their circulation time.[13] A recent study has shown that iron oxide nanoparticles in the form of nanoworms are internalized to a larger extent compared to spherical nanoparticles.[1] Thus, elongated iron oxide particles with high aspect ratio are expected to behave differently *in vivo* compared to their spherical counterparts. Anisotropic nanoparticles, when administered in the blood stream, can interfere to a larger extent with the blood vessel walls as shear forces push them towards the endothelium, and this might cause some defects.[6,14,15] The particle shape in conjunction with other particle characteristics, such as size, charge, and surface properties, plays an important role in phagocytosis by immune cells.[13] Thus, sufficiently elongated particles can avoid phagocytosis by macrophages.[13,16,17] Safari *et al.* observed significantly increased phagocytosis of rod-shaped particles by neutrophils and reduced phagocytosis by macrophages, monocytes and dendritic cells.[13,18] Understanding the correlation between the geometry of magnetic particles and their effects on cell membranes is a very challenging task the scientific community is facing.[1] Hinde *et al.* investigated how the shape

[a]*Faculty of Pharmacy, University of Ljubljana, 1000 Ljubljana, Slovenia. E-mail: slavko.kralj@ijs.si*
[b]*Department for Materials Synthesis, Jožef Stefan Institute, 1000 Ljubljana, Slovenia*
[c]*Nanos SCI, Nanos Scientificae d.o.o., Teslova 30, 1000 Ljubljana, Slovenia*
[d]*Institute of Cell Biology, Faculty of Medicine, University of Ljubljana, 1000 Ljubljana, Slovenia*

† Electronic supplementary information (ESI) available: Additional experimental details, materials and methods. See DOI: https://doi.org/10.1039/d2nr06965b

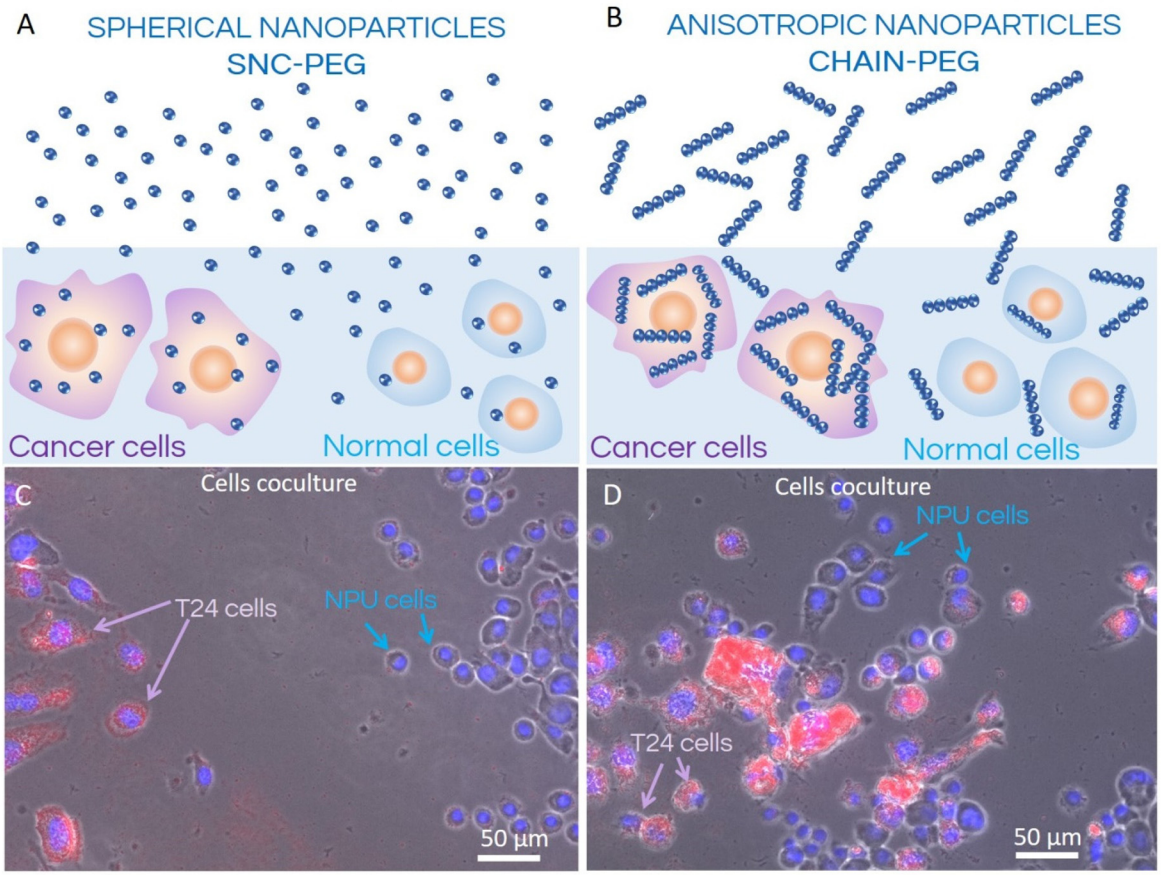

Fig. 1 Schematic representation (A and B) of the internalization process of spherical SNC-PEG (A) and anisotropic CHAIN-PEG (B) nanoparticles in co-culture of normal (NPU) and cancer (T24) urothelial cells and corresponding fluorescence microscopy images (C and D). T24 cancer cell nuclei are approximately two times larger than the nuclei of normal NPU cells; therefore, both cell types can easily be distinguished in the coculture. Both types of nanoparticles, spherical SNC-PEG and anisotropic CHAIN-PEG, were internalized preferentially into T24 cells whereas the extent of internalization of nanochains into T24 cells was larger compared to the spherical nanoparticles.

of nanoparticles influences the rate of intracellular transport. High aspect ratio nanoparticles, such as rods and worms, crossed cell barriers to different extents and generated different intracellular concentration gradients. This showed that particle shape can be a helpful trigger for achieving site-specific intracellular drug delivery.[13,19] Furthermore, it was shown that shape geometry also affects the site of nanoparticle accumulation *in vivo*. The non-spherical nanocarriers (*e.g.*, chains, disks, and rods), which show reduced phagocytosis, mostly exhibit lower accumulation in the liver and increased accumulation in other organs.[13,20–22]The final goal of research and development of magnetic nanoparticles is to produce magnetic nanoparticles, which would differentiate between healthy and cancer cells and hence be taken up preferentially by cancer cells (Fig. 1). The main issues in the development of such structures are related to difficulties with the design and synthesis of well-defined anisotropic superparamagnetic nanoparticles within the size range of a few tens of nanometers to one micrometer and with the control of their shape anisotropy.[4] The lack of systematic investigations of the effects of superparamagnetic nanoparticle shape anisotropy on cellular uptake is based on the fact that only a few research groups worldwide have mastered their complex synthesis.[5,23,24] The reason is related to the superparamagnetism of nanoparticles, which is preserved only when many spherical SPIONs are clustered into larger superparamagnetic nanoparticle clusters with a size of around 100 nm and not with the synthesis of individual iron-oxide nanocrystals with sizes larger than 20 nm.[25–28] Our group developed a dynamic assembly process, which is based on the magnetic alignment of nanoparticle clusters in suspension into chain-like nanostructures, *i.e.* nanochains, which are fixed by deposition of a silica layer (Fig. 2C and D). The process is highly adjustable and allows the preparation of anisotropic superparamagnetic particles with lengths of a few hundred nm and widths of ~100 nm, which are highly desirable for biomedical applications.[23,29,30]

Results and discussion

In this study, the effects of the shape anisotropy of superparamagnetic nanoparticles on their cellular response *in vitro* have

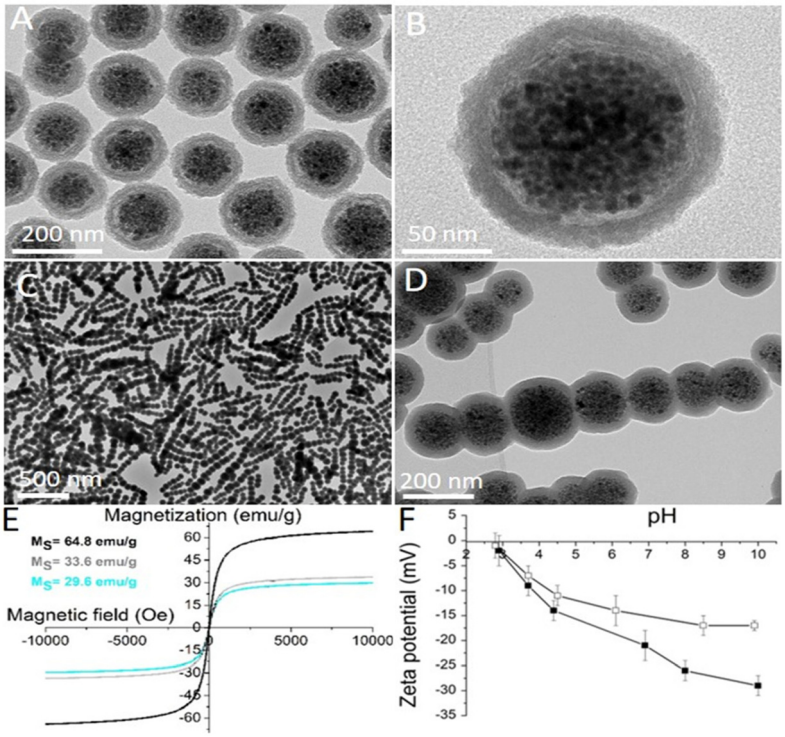

Fig. 2 Characterization data of the nanomaterials involved in the study. Representative transmission electron microscopy (TEM) image of spherical nanocrystal clusters coated with an amorphous silica shell and functionalized with PEG (SNC-PEG): (A) low and (B) high magnification. Representative TEM image of the CHAIN-PEG: (C) low and (D) high magnification. (E) Room-temperature measurements of the mass magnetization as a function of magnetic field for as-synthesized maghemite nanocrystals (black curve; MS = 64.8 emu g^{-1}), SNC-PEGs (grey curve; MS = 33.6.8 emu g^{-1}), and CHAIN-PEGs (cyan curve; MS = 29.6 emu g^{-1}). (F) The curves of the zeta potential as a function of pH for a suspension of SNCs (black squares) and SNC-PEGs (white squares).

been investigated. Thus, spherical and chain-like superparamagnetic nanoparticles were first designed and synthesized. The synthesis of the superparamagnetic nanocrystal clusters (SNCs) was based on the self-assembly of ~80 superparamagnetic iron oxide (maghemite) nanocrystals with a size of 10.4 ± 1.4 nm.[27] The size of the spherical SNCs coated with an approximately 25 nm thick silica shell and functionalized with polyethylene glycol (PEG) was 155 ± 18 nm (Fig. 2A and B). The silica shell was fluorescently labelled by rhodamine B isothiocyanate (RB), which was introduced during silica shell formation. RB reacted with amino silane prior to admixing tetraethoxysilane in order to form a covalent bond in a silica shell and thus avoid the uncontrolled release of free dye from the silica shell. Anisotropic superparamagnetic nanochains (CHAINs) functionalized with PEG (CHAIN-PEGs) were synthesized by the dynamic magnetic assembly of a few nanocrystal clusters (an average of 7 SNCs per CHAIN).[23] The transient and magnetically induced chain-like formations of SNCs in the suspension were fixed with the controlled deposition of a silica layer forming well-defined CHAINs. The core–shell nature of the nanochains, with the aligned nanocrystal cluster cores and amorphous silica shell, can be clearly distinguished in TEM micrographs (Fig. 2C and D). The mean length of CHAINs was ~800 nm and their cross diameter was ~150 nm. The SNC-PEGs and CHAIN-PEGs showed superparamagnetic properties (Fig. 2E) and high magnetic responsiveness.[4] When the suspension of such particles is exposed to a magnetic field gradient, the particles are rapidly separated from the suspension and, as soon as the external magnetic field is removed, the particles can be easily dispersed back to a stable suspension. The SNC-PEG and CHAIN-PEG suspensions showed good colloidal stability in aqueous dispersion with a pH value above 6 because there was no sedimentation detected in two months of monitoring. The zeta potential measurements of suspension of spherical SNC-PEG particles revealed a lower absolute value of zeta potential compared to SNCs with an unmodified surface, suggesting an efficient PEGylation of the particle surface (Fig. 2F). The presence of PEG chains on the surface of SNC-PEG and CHAIN-PEG nanoparticles was also confirmed by TGA (ESI, Fig. S1†).

XRD of the synthesized nanocrystals showed a single spinel phase, whereas Mössbauer spectroscopy confirmed that the nanocrystals were composed of maghemite, as reported in our previous manuscript.[27] The SNC-PEGs and CHAIN-PEGs exhibited superparamagnetic properties (Fig. 2E). Saturation magnetizations (Ms) of the synthesized nanocrystals, SNC-PEGs and CHAIN-PEGs, were 64.8, 33.9 and 29.6 emu g^{-1}, respectively (Fig. 2E). Hydrodynamic size measurements by

dynamic light scattering (DLS) were carried out only for spherical particles, namely SNCs and SNC-PEGs, because the size of CHAINs, due to their anisotropic shape, cannot be determined by DLS measurement protocols correctly. The mean hydrodynamic sizes of SNCs and SNC-PEGs in the A-DMEM/F12 cell culture medium were 206 nm (PDI 0.18) and 171 nm (PDI 0.19), respectively. After 24 h the mean hydrodynamic sizes of SNCs and SNC-PEGs in A-DMEM/F12 medium were 284 nm (PDI 0.16) and 156 nm (PDI 0.25), respectively. This shows that PEGylation contributed to the colloidal stability of magnetic nanoparticles in a complex medium. The mean hydrodynamic sizes of SNCs and SNC-PEGs in UroM ($+Ca^{2+}$ – SFBS) cell culture medium were 298 nm (PDI 0.15) and 226 nm (PDI 0.16), respectively. This indicates that the presence of calcium ions in UroM ($+Ca^{2+}$ – SFBS) medium adversely affected the hydrodynamic sizes of the dispersed nanoparticles.

The electrophoretic mobility of the spherical SNCs was measured as a function of the medium pH. The silica surface of SNCs showed a relatively acidic character because its structure comprised negatively charged hydroxyl groups at pH values above the isoelectric point at pH 2.8. The zeta potential of the SNCs reached a high negative value (−23 mV) at a physiological pH of 7.4 (Fig. 2F). Moreover, the zeta potential of the SNC-PEGs showed a slightly lower absolute value (−15 mV) compared to SNCs at a physiological pH (Fig. 2F), due to the presence of surface bound PEG chains. Relatively high absolute values of the zeta potential ensure strong electrostatic repulsive forces between particles, resulting in good colloidal stability of the nanoparticulate suspension in neutral and alkaline media. However, taking into account DLS and zeta potential measurements, the PEGylation ensured the steric stabilization of colloidal dispersion, since the mean hydrodynamic size of SNC-PEGs in cell culture media was smaller compared to that of SNCs. The zeta potential values of CHAINs in suspension were not analyzed due to their anisotropic shape and hence inconsistency with zeta potential measurement protocols. However, the zeta potential values of CHAINs are expected to be similar to those of the corresponding SNCs due to the same protocols being used for surface coating and functionalization of both nanomaterials.

Investigation of cellular uptake of fluorescently labelled nanoparticles has revealed different patterns for normal and cancer urothelial models. The cancer urothelial model of invasive neoplasm T24 cells (Fig. 3) showed a much higher fluo-

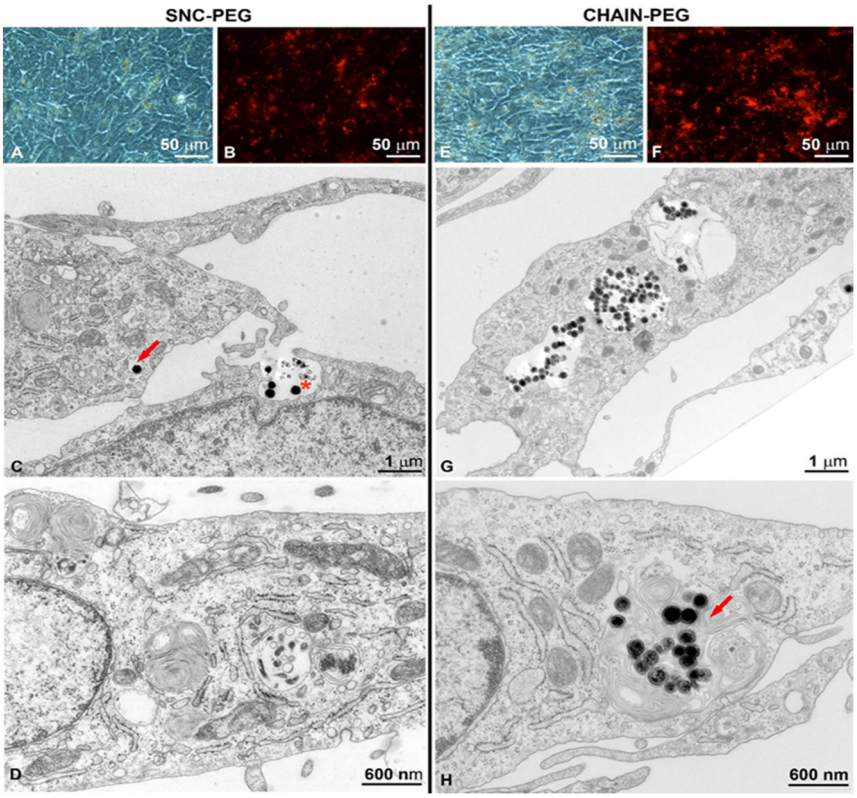

Fig. 3 (A and E) Phase-contrast microscopy, (B and F) fluorescence microscopy and (C, D, G and H) transmission electron microscopy images of cancer urothelial cells. Low magnification phase-contrast micrograph of cancer urothelial T24 cells treated with (A) SNC-PEGs and (E) CHAIN-PEGs. Areas rich in nanoparticles are visible as brown spots. Low magnification fluorescence micrograph of cancer urothelial T24 cells treated with (B) SNC-PEGs and (F) CHAIN-PEGs. Areas rich in nanoparticles are visible as red spots. TEM micrographs of cancer urothelial T24 cells treated with (C and D) SNC-PEGs and (G and H) CHAIN-PEGs. (C) SNC-PEGs are localized in the early endosome (red arrow). They are taken up by endocytosis as individual nanoparticles or small aggregates (asterisk), most likely by macropinocytosis. (D) SNC-PEG-free cell. (G) CHAIN-PEGs are intensely endocytosed and visible in endo-lysosomal compartments. (H) CHAIN-PEGs in the late endosome.

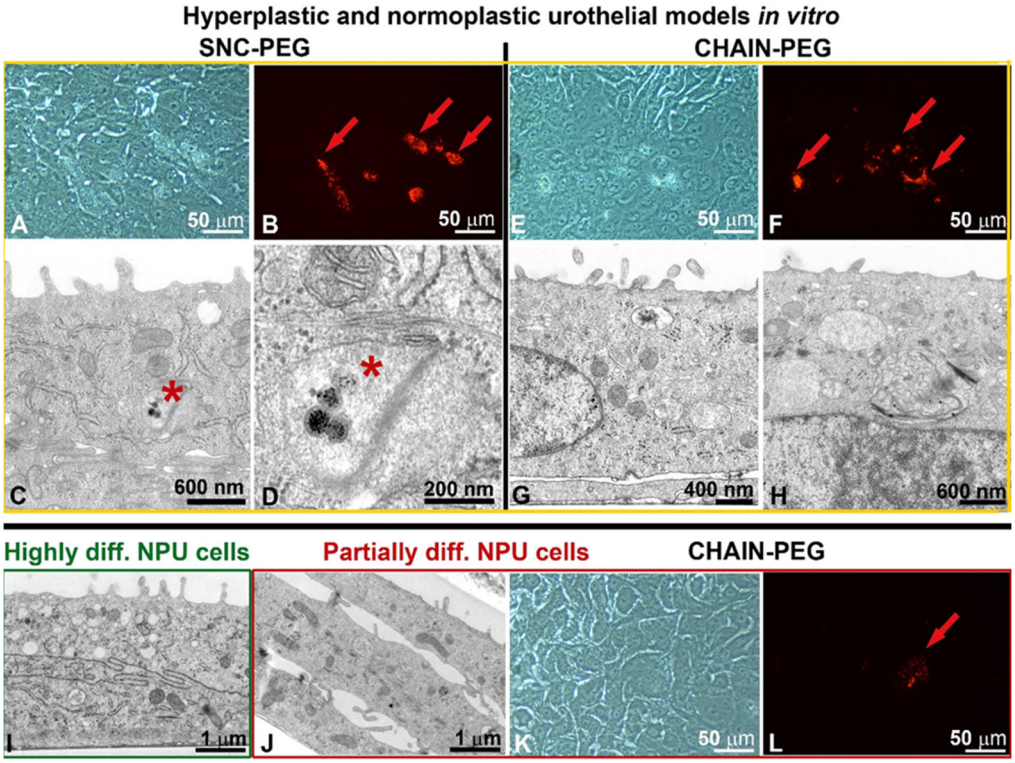

Fig. 4 (A, E and K) Phase-contrast microscopy, (B, F and L), fluorescence microscopy and (C, D, G, H, I and J) transmission electron micrographs of normal porcine urothelial (NPU) cells in hyperplastic (A–H, yellow framed images) or normoplastic (I–L, green and red framed images) urothelial models *in vitro*. Low magnification phase-contrast micrograph of partially differentiated NPU cells treated with (A) SNC-PEGs and (E) CHAIN-PEGs. Areas rich in nanoparticles are visible as brown spots. Low magnification fluorescence micrograph of partially differentiated NPU cells treated with (B) SNC-PEGs (red arrows) and (F) CHAIN-PEGs (red arrows). Areas rich in nanoparticles are visible as red spots (red arrows). Transmission electron micrographs of partially differentiated NPU cells treated with (C and D) SNC-PEGs and (G and H) CHAIN-PEGs. (C) SNC-PEGs are localized in the early endosome (asterisk). They are taken up by endocytosis as individual nanoparticles. Image (D) is an enlarged section of image C. (G and H) CHAIN-PEG-free cells. (I) Neither SNC-PEGs nor CHAIN-PEGs are visible in highly differentiated NPU cells. (J) Transmission electron microscopy, (K) phase-contrast microscopy, (L) fluorescence microscopy of partially differentiated NPU cells (green framed image) in the normoplastic urothelial model. (K and L) Only in one partially differentiated NPU cell are the CHAIN-PEGs visible (red arrow, red frame). No CHAIN-PEGs are visible at the ultrastructural level in partially differentiated NPU cells of the normoplastic urothelial model (red framed images).

rescence intensity compared to the normal urothelial model with partially (Fig. 4) and highly differentiated NPU cells (Fig. 5), indicating a higher uptake of nanoparticles into cancer cells. This is consistent with our previous studies on the uptake of rhodamine B-labelled polyacrylic acid-coated cobalt ferrite nanoparticles in biomimetic urothelial *in vitro* models.[31]

The number of internalized SNC-PEGs (*i.e.* areas containing SNC-PEGs) was lower than the number of internalized CHAIN-PEGs (*i.e.* areas with CHAIN-PEGs), 561 and 5105, respectively. The apparent average particle size was 38 px for SNC-PEGs and 139 px for CHAIN-PEGs. The image surface area covered by the SNC-PEG particles was 0.43% and that covered by the CHAIN-PEG particles was 14%. Transmission electron microscopy (TEM) enabled us to distinguish between internalized nanoparticles and nanoparticles caught in the intercellular space (Fig. 3). SNC-PEGs were observed in the intercellular space of the T24 urothelial model and only occasionally were they found internalized. Cells without SNC-PEGs were predominantly detected. In the cancer urothe-

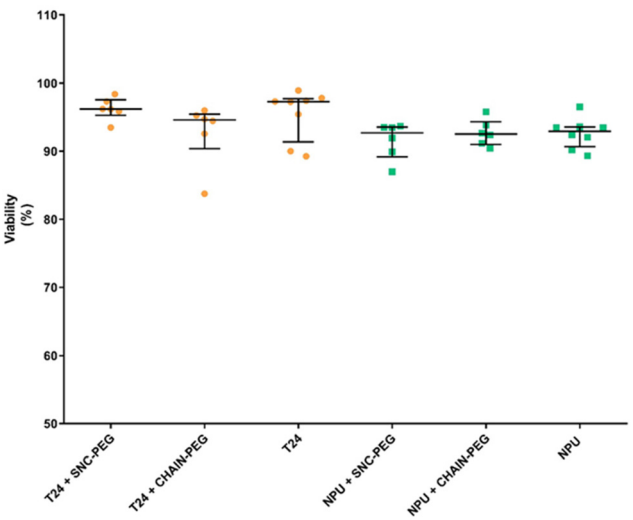

Fig. 5 Viability of cancer (T24) and normal (NPU) urothelial cells after 24 h of exposure to 100 µg mL^{-1} of SNC-PEG or CHAIN-PEG. The results are presented as percentages of viable cells in the cell culture.

Table 1 Cell viability and ICP-OES analysis

Sample	Cell viability (% ± SE)	C_{Fe} (μg mL^{-1})	Corrected C_{Fe} (μg mL^{-1})	Total mass of Fe (μg) based on corrected C_{Fe}	Calculated mean mass of Fe (×10^{-13} g) per cell
NPU	98.0 ± 0.3	<0.10	—	—	—
NPU + SNC-PEG	88.6 ± 0.2	<0.10	0	—	—
NPU + CHAIN-PEG	94.3 ± 0.3	<0.10	0	—	—
T24	94.3 ± 1.3	0.19 ± 0.05	—	—	—
T24 + SNC-PEG	91.4 ± 0.3	0.49 ± 0.00	0.30 ± 0.05	3.60 ± 0.60	2.276
T24 + CHAIN-PEG	90.5 ± 1.5	0.74 ± 0.02	0.55 ± 0.05	6.60 ± 0.60	3.561

lial model, SNC-PEGs and CHAIN-PEGs were taken up by endocytosis (Fig. 3C, G and H) and underwent the intracellular endo-lysosomal pathway, as suggested by the nanoparticles observed in different endosomal compartments (Fig. 3C, early endosome, red arrow and Fig. 3H, late endosome, red arrow). Neither SNC-PEGs nor CHAIN-PEGs were found to be free in the cytosol or in association with any other intracellular organelle.

The internalization of SNC-PEGs or CHAIN-PEGs was rare and detected only in some partially differentiated normal urothelial cells of the hyperplastic urothelial model *in vitro* (Fig. 4A–H, red arrows in B and F, and asterisks in C and D) and only in one cell were the CHAIN-PEGs visible in a normoplastic urothelial model in which very few NPU cells were partially differentiated (Fig. 4J–L, red arrow in L). No SNC-PEGs or CHAIN-PEGs were found in highly differentiated urothelial cells (Fig. 4I), which is consistent with our previous findings that the endocytotic activity of bladder urothelial cells is inversely related to their differentiation stage.[31–35]

In order to further quantitatively determine the amount of Fe in each sample, inductively coupled plasma optical emission spectroscopy (ICP-OES) analysis was performed, and the obtained values are listed in Table 1. The highest mean value of Fe content was detected in cancer urothelial cells T24 + CHAIN-PEG, which was 3.561 × 10^{-13} g per cell, followed by T24 + SNC-PEG (2.276 × 10^{-13} g per cell). The iron content in NPU cells treated with nanoparticles was below the detection limit in all analyzed samples. It is known that magneto-liposomes containing magnetic nanoparticles in the bilayer are preferentially taken up by cancerous T24 cells, which leads to an improvement in the contrast and an easier distinction between the healthy and cancerous cells.[36]

In summary, we have presented the results obtained *in vitro* in biomimetic and co-culture models. These results are extremely important as we additionally show the ultrastructure of the cells and also the localization of the nanoparticles in cancer cells and partially differentiated normal urothelial cells (Fig. 3 and 4). Furthermore, the fluorescence images supplemented with TEM, the comparison of NP uptake into normal and cancer cells in co-culture and finally the ICP-MS analysis clearly show the differences in the internalization of magnetic nanoparticles of different shapes in cancer cells (Fig. 1) This is in line with a previous study which reported that the route of particle internalization depends on the particle shape.[37]

The investigation of the effects of magnetic nanoparticles on cell viability revealed that after 24 h of exposure, the presence of both types of magnetic nanoparticles, namely SNC-PEG and CHAIN-PEG, did not affect the viability of either normal or cancer urothelial cells (Fig. 5). Thus, our results clearly demonstrate that nanochains are not toxic to cells *in vitro* and preferentially accumulate in cancer cells. These findings are very promising for potential novel application development using the presented features of nanochains. The exposure of nanochains to a low frequency rotating magnetic field has been reported to enable the control of drug delivery where rotational movements of nanochains accelerate the release of carried drugs which cause synergistic effects in cancer treatment.[5] Interestingly, similar chain-like magnetic particles (magnetosome chains) are also found in nature in some organisms as simple as magnetotactic bacteria.[38] They use these magnetic assemblies for their navigation in a geomagnetic field. However, there are some important differences between our artificial nanochains and the magnetosome chains in terms of magnetic properties and the possibility of surface functionalization as demonstrated in our recent review.[38] The application of magnetosome chains in biomedicine is still under investigation, but the millions of years of their evolution indicate the intracellular compatibility of such magnetic nano-assemblies, and the acceptance and exploitation of anisotropic magnetic nanostructures by living organisms.

Conclusions

In summary, we designed and synthesized anisotropic magnetic nanochains and investigated the effects of magnetic nanoparticles' shape anisotropy on cellular uptake. Currently, the effects of nanoparticles' shape anisotropy on cellular uptake are still poorly understood due to challenges in the synthesis of anisotropic magnetic nanoparticles of the same composition. Here, we investigated the cellular uptake of differently shaped magnetic nanoparticles in urothelial cells *in vitro*. Although both shapes of nanomaterials reveal biocompatibility, we have found significant differences in the extent of their intracellular accumulation. Contrary to spherical particles, anisotropic nanochains preferentially accumulate in cancer cells, indicating that control of nanoparticle shape geometry governs cell-type selective intracellular uptake and accumulation. Our

findings thus open a new perspective for potential selective cancer treatment utilizing the differences in nanoparticle shape anisotropy.

Author contributions

T.P.: investigation and, writing of the original draft. S.K.: resources, conceptualization, methodology, investigation, writing – review & editing, and supervision. S.N.: investigation. P.K.: conceptualization, methodology, and writing – review & editing, and supervision. M.E.K.: conceptualization, methodology, investigation, and writing – review & editing. The manuscript was written through contributions from all authors. All authors have given approval to the final version of the manuscript.

Conflicts of interest

There are no conflicts to declare.

Acknowledgements

The authors gratefully acknowledge the financial support provided by the Slovenian Research Agency (ARRS Program Codes P1-0189, P1-0420, P2-0089, and P3-0108 and Projects J2-3043, J2-3040, J2-3046, J3-3079, J1-7302, J7-4420 and J7-2594, and bilateral ARRS project: BI-FR/23-24-PROTEUS-005) and the MRIC UL IP-0510 Infrastructure program. We thank Linda Štrus, Nada Pavlica, Sanja Čabraja and Sabina Železnik for technical help and Prof. Odon Planinšek for critical discussion on TGA analysis. We acknowledge the CENN Nanocenter (Ljubljana, Slovenia) for access to TEM.

References

1 A. G. Roca, L. Gutiérrez, H. Gavilán, M. E. Fortes Brollo, S. Veintemillas-Verdaguer and M. del P. Morales, *Adv. Drug Delivery Rev.*, 2019, **138**, 68–104.
2 Č. Dragar, S. Kralj and P. Kocbek, *Int. J. Pharm.*, 2021, **597**, 120348.
3 M. Musielak, I. Piotrowski and W. M. Suchorska, *Rep. Pract. Oncol. Radiother.*, 2019, **24**, 307–314.
4 S. Nemec, S. Kralj, C. Wilhelm, A. Abou-Hassan, M.-P. Rols and J. Kolosnjaj-Tabi, *Appl. Sci.*, 2020, **10**, 7322.
5 L. Wan, H. Song, X. Chen, Y. Zhang, Q. Yue, P. Pan, J. Su, A. A. Elzatahry and Y. Deng, *Adv. Mater.*, 2018, **30**, 1707515.
6 C. Naud, C. Thébault, M. Carrière, Y. Hou, R. Morel, F. Berger, B. Diény and H. Joisten, *Nanoscale Adv.*, 2020, **2**, 3632–3655.
7 M. Cooley, A. Sarode, M. Hoore, D. A. Fedosov, S. Mitragotri and A. Sen Gupta, *Nanoscale*, 2018, **10**, 15350–15364.
8 Z. Zhou, X. Ma, E. Jin, J. Tang, M. Sui, Y. Shen, E. A. Van Kirk, W. J. Murdoch and M. Radosz, *Biomaterials*, 2013, **34**, 5722–5735.
9 A. L. van de Ven, P. Kim, O. Haley, J. R. Fakhoury, G. Adriani, J. Schmulen, P. Moloney, F. Hussain, M. Ferrari, X. Liu, S.-H. Yun and P. Decuzzi, *J. Controlled Release*, 2012, **158**, 148–155.
10 D. A. Christian, S. Cai, O. B. Garbuzenko, T. Harada, A. L. Zajac, T. Minko and D. E. Discher, *Mol. Pharm.*, 2009, **6**, 1343–1352.
11 S. Shukla, A. L. Ablack, A. M. Wen, K. L. Lee, J. D. Lewis and N. F. Steinmetz, *Mol. Pharm.*, 2013, **10**, 33–42.
12 S. Kralj, T. Potrc, P. Kocbek, S. Marchesan and D. Makovec, *Curr. Med. Chem.*, 2017, **24**, 454–469.
13 N. Kapate, J. R. Clegg and S. Mitragotri, *Adv. Drug Delivery Rev.*, 2021, **177**, 113807.
14 E. Carboni, K. Tschudi, J. Nam, X. Lu and A. W. K. Ma, *AAPS PharmSciTech*, 2014, **15**, 762–771.
15 H. Ye, Z. Shen, L. Yu, M. Wei and Y. Li, *Proc. R. Soc. A*, 2018, **474**, 20170845.
16 J. A. Champion and S. Mitragotri, *Pharm. Res.*, 2009, **26**, 244–249.
17 D. M. Richards and R. G. Endres, *Rep. Prog. Phys.*, 2017, **80**, 126601.
18 H. Safari, W. J. Kelley, E. Saito, N. Kaczorowski, L. Carethers, L. D. Shea and O. Eniola-Adefeso, *Sci. Adv.*, 2020, **6**(24), 1474.
19 E. Hinde, K. Thammasiraphop, H. T. T. Duong, J. Yeow, B. Karagoz, C. Boyer, J. J. Gooding and K. Gaus, *Nat. Nanotechnol.*, 2017, **12**, 81–89.
20 Y. Zhao, Y. Wang, F. Ran, Y. Cui, C. Liu, Q. Zhao, Y. Gao, D. Wang and S. Wang, *Sci. Rep.*, 2017, **7**, 4131.
21 P. M. Peiris, L. Bauer, R. Toy, E. Tran, J. Pansky, E. Doolittle, E. Schmidt, E. Hayden, A. Mayer, R. A. Keri, M. A. Griswold and E. Karathanasis, *ACS Nano*, 2012, **6**, 4157–4168.
22 P. Decuzzi, B. Godin, T. Tanaka, S.-Y. Lee, C. Chiappini, X. Liu and M. Ferrari, *J. Controlled Release*, 2010, **141**, 320–327.
23 S. Kralj and D. Makovec, *ACS Nano*, 2015, **9**, 9700–9707.
24 J. Kolosnjaj-Tabi, S. Kralj, E. Griseti, S. Nemec, C. Wilhelm, A. Plan Sangnier, E. Bellard, I. Fourquaux, M. Golzio and M.-P. Rols, *Cancers*, 2019, **11**, 2040.
25 P. Kocbek, S. Kralj, M. E. Kreft and J. Kristl, *Eur. J. Pharm. Sci.*, 2013, **50**, 130–138.
26 S. Kralj and D. Makovec, *RSC Adv.*, 2014, **4**, 13167.
27 M. Tadic, S. Kralj, M. Jagodic, D. Hanzel and D. Makovec, *Appl. Surf. Sci.*, 2014, **322**, 255–264.
28 S. Piovesana, D. Iglesias, M. Melle-Franco, S. Kralj, C. Cavaliere, M. Melchionna, A. Laganà, A. L. Capriotti and S. Marchesan, *Nano Res.*, 2020, **13**, 380–388.
29 M. Tadic, S. Kralj, Y. Lalatonne and L. Motte, *Appl. Surf. Sci.*, 2019, **476**, 641–646.
30 M. Tadic, S. Kralj and L. Kopanja, *Mater. Charact.*, 2019, **148**, 123–133.

31 J. Lojk, V. B. Bregar, K. Strojan, S. Hudoklin, P. Veranič, M. Pavlin and M. E. Kreft, *Histochem. Cell Biol.*, 2018, **149**, 45–59.
32 M. E. Kreft, R. Romih, M. Kreft and K. Jezernik, *Differentiation*, 2009, **77**, 48–59.
33 M. Pavlin, J. Lojk, V. B. Bregar, M. Rajh, K. Mis, M. E. Kreft, S. Pirkmajer and P. Veranic, *Int. J. Nanomed.*, 2015, 1449.
34 L. Tratnjek, R. Romih and M. E. Kreft, *Histochem. Cell Biol.*, 2017, **148**, 143–156.
35 D. Zupančič, M. E. Kreft, M. Grdadolnik, D. Mitev, A. Iglič and P. Veranič, *Protoplasma*, 2018, **255**, 419–423.
36 N. Kostevšek, C. C. L. Cheung, I. Serša, M. E. Kreft, I. Monaco, M. Comes Franchini, J. Vidmar and W. T. Al-Jamal, *Nanomaterials*, 2020, **10**, 889.
37 N. Hao, L. Li, Q. Zhang, X. Huang, X. Meng, Y. Zhang, D. Chen, F. Tang and L. Li, *Microporous Mesoporous Mater.*, 2012, **162**, 14–23.
38 S. Kralj and S. Marchesan, *Pharmaceutics*, 2021, **13**, 1262.